Persistent polyamorphism in the chiton tooth: From a new biomineral to inks for additive manufacturing

Linus Stegbauer[a,1], Paul J. M. Smeets[a,2], Robert Free[a], Shay G. Wallace[a], Mark C. Hersam[a], Esen E. Alp[b], and Derk Joester[a,3]

[a]Materials Science and Engineering, Northwestern University, Evanston, IL 60208; and [b]Advanced Photon Source, Sector 3, Argonne National Laboratory, Lemont, IL 60439

Edited by Patricia M. Dove, Virginia Tech, Blacksburg, VA, and approved April 19, 2021 (received for review September 28, 2020)

Engineering structures that bridge between elements with disparate mechanical properties are a significant challenge. Organisms reap synergy by creating complex shapes that are intricately graded. For instance, the wear-resistant cusp of the chiton radula tooth works in concert with progressively softer microarchitectural units as the mollusk grazes on and erodes rock. Herein, we focus on the stylus that connects the ultrahard and stiff tooth head to the flexible radula membrane. Using techniques that are especially suited to probe the rich chemistry of iron at high spatial resolution, in particular synchrotron Mössbauer and X-ray absorption spectroscopy, we find that the upper stylus of *Cryptochiton stelleri* is in fact a mineralized tissue. Remarkably, the inorganic phase is nano disperse santabarbaraite, an amorphous ferric hydroxyphosphate that has not been observed as a biomineral. The presence of two persistent polyamorphic phases, amorphous ferric phosphate and santabarbaraite, in close proximity, is a unique aspect that demonstrates the level of control over phase transformations in *C. stelleri* dentition. The stylus is a highly graded material in that its mineral content and mechanical properties vary by a factor of 3 to 8 over distances of a few hundred micrometers, seamlessly bridging between the soft radula and the hard tooth head. The use of amorphous phases that are low in iron and high in water content may be key to increasing the specific strength of the stylus. Finally, we show that we can distill these insights into design criteria for inks for additive manufacturing of highly tunable chitosan-based composites.

biomineralization | chiton | polyamorphism | amorphous ferric hydroxyphosphate | additive manufacturing

Biominerals are broadly used by organisms to reinforce structural materials, enabling for instance locomotion, feeding, and defense but also finding application in sensing (1). A defining principle of mineralized tissues is their composite nature, reaping synergy from the combination of a soft macromolecular matrix and a hard, inorganic mineral phase (2, 3). Organisms functionally grade such composites by precisely controlling the phase, size, shape, orientation, dispersion, and spatial distribution of mineral nanoparticles. Harnessing the biological capability to create composites that combine complex shape with mechanical properties that are graded intricately yet over several orders of magnitude in range is of interest for a broad range of functional materials—for instance, for soft robotics (4).

Chitons, a class of marine mollusks, are best known for the extreme hardness, rich chemistry, and intricate phase assemblage of their radula teeth (Fig. 1 and *SI Appendix*, Fig. S1, for recent reviews see refs. 5 and 6; for a cross-cutting review that includes chiton biominerals, see ref. 7). However, the mechanical system of their dentition is not only significantly more complex but also based on a continuous organic phase that is differentially reinforced. The chiton therefore serves as an excellent model system to study biological mechanisms and design principles.

The chiton radula is slender ribbon with transverse rows of teeth (Fig. 1 *B*–*D*) (9). Two outsize major lateral teeth make contact with the substrate during grazing. Major lateral teeth consist of a tooth head and stylus (Fig. 1 *D* and *E* and *SI Appendix*, Figs. S1 and S10) that is anchored on the radula membrane (10, 11). The stylus canal runs along the length of the hollow stylus and terminates in a dead end below the junction zone between stylus and cusp. During the feeding stroke, the radula slides over a curved supporting surface and bends in two orthogonal directions. This results in a characteristic scraping and sweeping motion of radula teeth (12). The loss of entire rows of teeth due to wear is compensated for by synthesis of new teeth at the posterior end (13, 14). Newly formed teeth mature in several stages as they are transported toward the anterior end by the radula membrane (15). As a result, their entire development can be observed in one animal (Fig. 1*C*).

The function of the radula requires highly disparate material properties. The tooth complex is based on a continuous organic scaffold comprised of semicrystalline, partially deacetylated α-chitin and protein and may be crosslinked by tanning reactions (16). The tooth head is comprised of a highly mineralized cusp with exceptional hardness, wear resistance, and self-sharpening properties (17). The cusp is supported by a softer core. In *Cryptochiton*-type teeth, magnetite covers the entire posterior surface (leading edge) of the cusp and all but a rectangular

CHEMISTRY

Significance

Biomineralization is a highly successful strategy to create functionally graded materials with complex shape. Herein, we demonstrate that the rock-grazing mollusk *Cryptochiton stelleri* uses two amorphous, yet structurally distinct, phases in neighboring microarchitectural domains to reinforce its dentition. Nano-disperse santabarbaraite, an amorphous iron hydroxyphosphate, is present in the stylus, extending the range over which hardness and stiffness vary by at least a factor of two. Use of ferric phosphates with low iron and high water content may present a stratagem to create strong composites with low density. Indeed, we show that bio-inspired inks based on chitosan and mineral precursors allow three-dimensional printing of tunable composites strengthened by amorphous nanoparticles precipitated in situ.

Author contributions: L.S., P.J.M.S., R.F., S.G.W., M.C.H., E.E.A., and D.J. designed research; L.S., P.J.M.S., R.F., S.G.W., and E.E.A. performed research; L.S., P.J.M.S., R.F., S.G.W., E.E.A., and D.J. analyzed data; and L.S., P.J.M.S., R.F., S.G.W., M.C.H., E.E.A., and D.J. wrote the paper.

The authors declare no competing interest.

This article is a PNAS Direct Submission.

Published under the PNAS license.

[1]Present address: Institute of Interfacial Process Engineering and Plasmatechnology, University of Stuttgart, 70569 Stuttgart, Germany.

[2]Present address: Northwestern University Atomic and Nanoscale Characterization Experimental Center, Northwestern University, Evanston, IL 60208.

[3]To whom correspondence may be addressed. Email: d-joester@northwestern.edu.

This article contains supporting information online at https://www.pnas.org/lookup/suppl/doi:10.1073/pnas.2020160118/-/DCSupplemental.

Published June 4, 2021.

Downloaded at Universiteit Gent on June 10, 2021

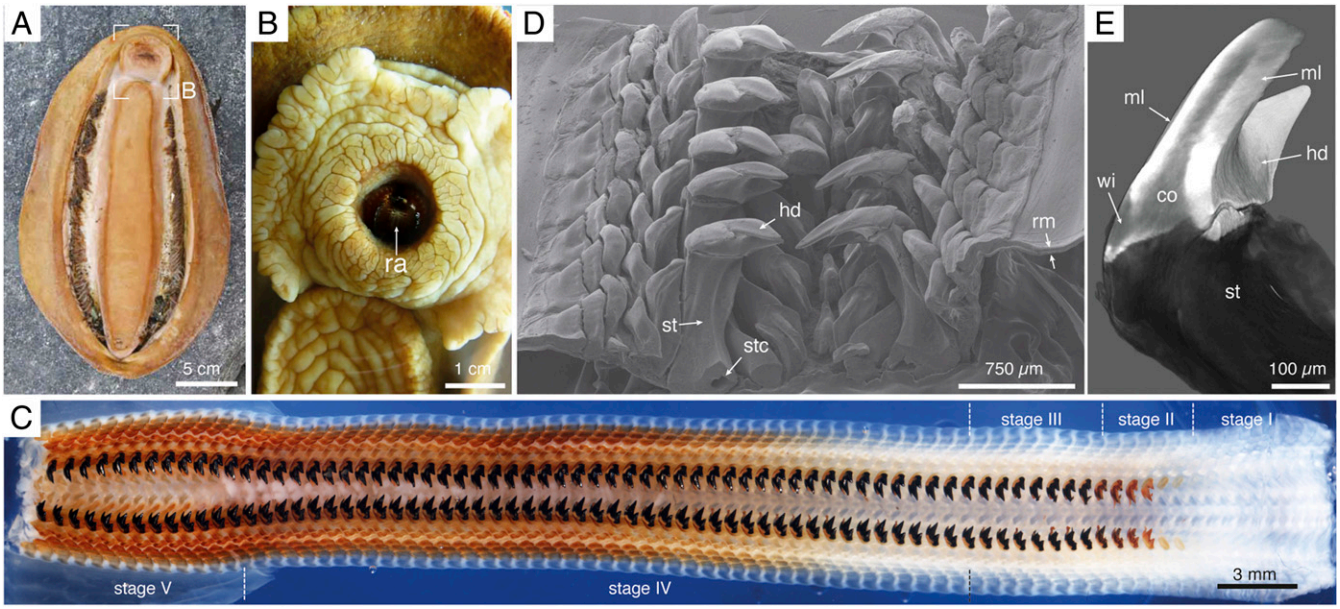

Fig. 1. Radula teeth of *C. stelleri*. (*A*) Ventral aspect of *C. stelleri* [Image credit: Linda Schroeder (photographer)]. (*B*) Mouth and protruding anterior end of radula (ra) (8). Image credit: VicHigh Marine/David Young. (*C*) Mosaic image of the entire radula showing all stages of development, including deposition of the organic scaffold (stage I), infiltration of the cusp with ferrihydrite (stage II), conversion to magnetite (stage III), mineralization of the core (stage IV), and mature teeth (stage V). (*D*) SEM image of the anterior end of the radula with mature teeth. Major lateral teeth consist of the tricuspidate head (hd, 400 × 350 × 150 μm^3) and the stylus (st, L-shape 1,400 × 1,400 × 350 μm^3). The stylus anchors teeth on the thin (~100 μm; *SI Appendix*, Fig. S10*C*) and flexible radula membrane (rm). The stylus canal (stc) runs along the length of the stylus but terminates below the head. (*E*) Rendering of a virtual section of a tooth head (hd) and upper stylus (st) generated from a 3D reconstruction of the normalized linear attenuation coefficient (LAC) as determined by synchrotron microcomputed tomography. Note the LAC is highest for the outer magnetite layer (ml) of the head, intermediate for AFP-based composite of the core (co), and rather low in the stylus. Typical for *Cryptochiton* type teeth, the core is exposed in a window (wi) in the magnetite layer on the trailing (anterior) face of the tooth.

window on the anterior surface (trailing edge) (5). The biomineral of the tooth core, amorphous ferric phosphate (AFP), is thus exposed in the window (Fig. 1*E* and *SI Appendix*, Fig. S1) (18). Use of at least two biominerals is typical for chiton teeth, and a considerable number has been identified in the core of different species (see ref. 5 and references therein). Additionally, ferrihydrite occurs as a transient precursor phase in stage II of radula development (Fig. 1*C*) (18).

The entire head is mounted on the stylus, an L-shaped chitinous tissue that is integral to the complex movement of the

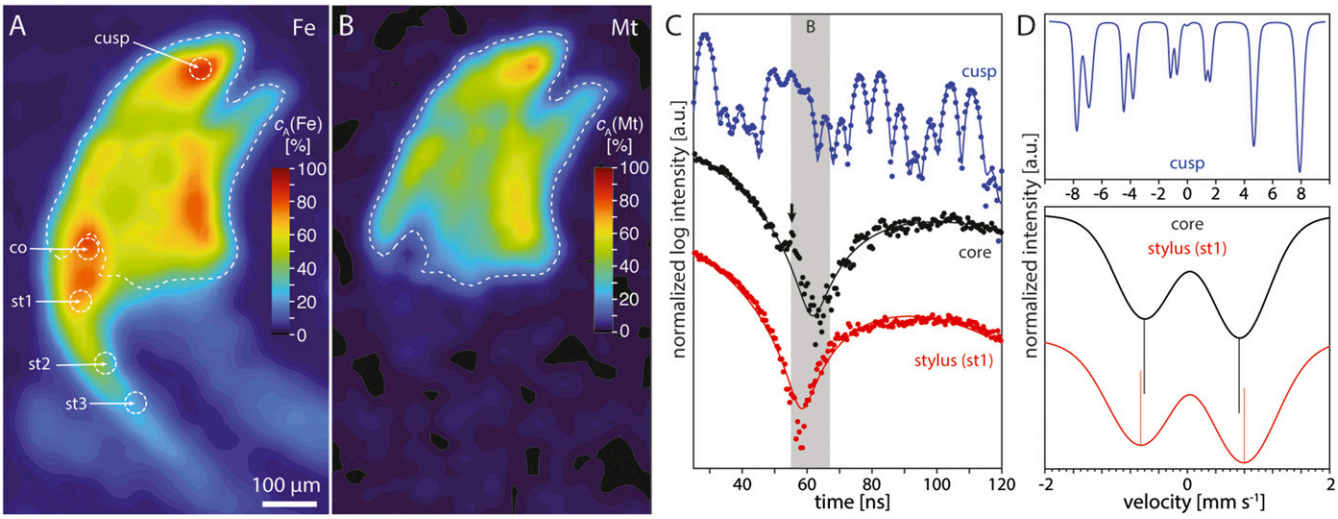

Fig. 2. Phase assemblage of major lateral teeth of *C. stelleri*. (*A*) Contour map of the normalized area concentration (c_A) of iron, based on SMS resonance intensity, across a longitudinal section (thickness ~150 μm) of a mature tooth head and upper stylus. (*B*) Phase-selective map of the magnetite (Mt) distribution generated by accumulating intensity only for times between 55 and 67 ns, as indicated by the shaded area in *C*. Mt concentration was below the detection limit outside the dashed contour line. (*C*) SMS point spectra of the cusp, core, and stylus site 1 (st1) were taken at the sites indicated by dashed circles in *A*; for spectra from sites st2 and st3, please refer to *SI Appendix*, Fig. S12. Models fit to the data are indicated by solid lines of corresponding color. Deviation of the core spectra from the fit (black arrow) are due to the presence of a small fraction of magnetite. (*D*) Velocity domain Mössbauer spectra were simulated based on parameters fitted to the spectra in *C*. Location of minima for core and stylus (st1) are indicated by vertical lines.

Downloaded at Universiteit Gent on June 10, 2021

tooth head during the feeding stroke (Fig. 1*D* and *SI Appendix*, Fig. S10 *A* and *B*) (19). The stylus connects the tooth head to the radula and orients the tooth with respect to the substratum (20). The radula membrane (Fig. 1*D* and *SI Appendix*, Fig. S10*C*) has lower stiffness to accommodate complex shape changes but at the same time must be strong, tough, and resistant to fatigue to survive the cycling bending and unbending during feeding. As a consequence of these vastly different requirements, we expect that mechanical properties are strongly graded. This is well documented for the cusp and core of radula teeth but less explored for the stylus and radula (17, 21, 22).

The stylus and the radula membrane are generally referred to as unmineralized tissues, even though the presence of transient mineral has been suggested and the junction zone does mineralize in later stages (5, 22). However, the chemical form in which iron appears in the junction zone and stylus remains unclear. We therefore set out to map the redox state and chemical environment of iron in the tooth of *Cryptochiton stelleri* with the long-term goal to trace these parameters over the development of the radula and thus gain insight into the mechanisms at play. This would then provide a foothold on the way to designing bio-inspired syntheses.

Given the complex shape (Fig. 1 *D* and *E*) and small size of chiton teeth and the extraordinarily rich chemistry of iron, mapping of multiple, often poorly crystalline phases requires techniques that combine high spatial resolution with sensitivity for subtle differences in oxidation state and coordination geometry of iron. Synchrotron Mössbauer spectroscopy (SMS) recently emerged as a powerful tool that combines high spatial resolution with the deep chemical insights offered by classical Mössbauer spectroscopy (23–25). Herein, we report on our discovery of a biomineral in the mature upper stylus of *C. stelleri* using SMS and correlative imaging and spectroscopy techniques.

Results and Discussion

The resonance intensity in SMS is proportional to the total amount of ^{57}Fe in the interaction volume. Intensity maps therefore report on the projected (area) concentration of iron (Fig. 2*A*). The distribution of iron across a major lateral tooth indicates that the section contains not only part of the major cusp but also a piece of a minor cusp, similar to the virtual section through a three-dimensional (3D) reconstruction generated by synchrotron microcomputed tomography (Fig. 1*E* and *SI Appendix*, Fig. S1).

SMS spectra recorded at the tip of the central cusp show a characteristic oscillation in the scattered intensity within a short time window after excitation (Fig. 2*C*, blue circles). The periods and amplitudes of this "quantum beat" contain valuable information regarding the environment of iron atoms. This information can be extracted by fitting the spectra with a suitable model (blue line). Consistent with expectations, we find that the model for the cusp requires specifying two distinct iron sites, one representing octahedrally coordinated and the other tetrahedrally coordinated iron (*SI Appendix*, Table S1). Fit parameters include two quadrupole splitting components (Δ_1 and Δ_2) that result from electric field gradients and two hyperfine field components (B_1 and B_2) that are caused by the magnetic field in magnetite. Using these fit parameters, we simulated the classical velocity (energy) domain Mössbauer spectrum and find that it matches expectations for magnetite (Fig. 2*D*, blue) (26).

Point spectra taken from the region at the base of the trailing edge of the major cusp, where we expect the window in the magnetite layer, and on into the stylus have a characteristic, broad V-shape (Fig. 2*C* and *SI Appendix*, Fig. S14). Using the logarithmic scaling of the intensity to our advantage, we identified a time window (55 to 67 ns) in which nuclear scattering from magnetite dominates the detected intensity (shaded area in Fig. 2*C*). This allowed us to construct a phase-selective map for magnetite (Fig. 2*B*). Inspection of this map confirms that the first sampling site corresponds to the tooth core close to the magnetite layer. Based on distances, the three other sites all fall into the stylus.

Spectra for the core and the first stylus site were fit with one quadrupole splitting component each (Δ, *SI Appendix*, Table S2). In the velocity domain, simulated spectra of the core (Fig. 2*D*) closely resemble those of synthetic AFP ($\Delta = 0.67\ \mathrm{mm \cdot s^{-1}}$) (27), with broad resonances typical for amorphous phases (full width at half maximum, $\mathrm{FWHM}_\Delta = 0.79\ \mathrm{mm \cdot s^{-1}}$). A small residual in core spectra most likely corresponds to the presence of a small amount (10 to 15%) of magnetite. While spectra of the upper stylus are superficially similar to those of AFP, they are distinct in that the minimum in the time domain is shifted toward shorter delay times (Fig. 2*C* and *SI Appendix*, Fig. S14). Fitting reveals that the quadrupole splitting is larger ($\Delta = 0.72\ \mathrm{mm \cdot s^{-1}}$), and the line width is even broader ($\mathrm{FWHM}_\Delta = 0.88\ \mathrm{mm \cdot s^{-1}}$). Given that the uncertainty for both fit parameters is less than 10% of the difference between their values for the core and the stylus (*SI Appendix*, Table S2), it seems likely that the suggestion that a chemically distinct phase is present in the stylus is correct (22). Based on the large line width, this phase is likely amorphous and/or occurs in rather small particles. Indeed, while the reflections of α-chitin are readily apparent in X-ray diffraction patterns of the stylus, there is no indication of any other crystalline phase (*SI Appendix*, Fig. S3).

Conventional Mössbauer spectra of a radula from which the tooth heads, but not styli, had been removed are very similar to the simulated spectra of the stylus (*SI Appendix*, Figs. S13 and S14 cf. Fig. 2*D*). Fitting reveals that quadrupole splitting and line width match those of the transition observed for the unknown biomineral in the stylus (*SI Appendix*, Table S3). Slightly enhanced line width leaves open the possibility that additional phases may be present (for instance in the lower stylus or elsewhere in the radula), but if so, these are likely amorphous as well. This bulk experiment further reported an isomer shift $\delta = 0.39\ \mathrm{mm \cdot s^{-1}}$, indicating that all iron detected in stylus and radula is present as Fe(III). Based on the quadrupole splitting, Fe(III) in the stylus occurs in octahedral coordination and in a high-spin state (28).

Wanting to eliminate the possibility that the stylus is comprised of a mixture of AFP and either ferrihydrite, a precursor phase found in all chitons, lepidocrocite, one of the iron oxyhydroxides that is found in *Acanthopleura* type teeth, or goethite (29), a polymorph of lepidocrocite observed in the limpet, and a number of other purely oxidic phases with μ-hydroxo–linked polymers of FeO_6 octahedra, we looked for evidence of magnetic splitting below the characteristic blocking temperature (*SI Appendix*, Fig. S14). With no such evidence in SMS spectra down to 54 K, it appears unlikely that any of these phases is present (29), unless complexation with organic ligands depresses the blocking temperature below typical values (30). While we do not know whether there are such ligands in the stylus, a comparison of Fourier-transform infrared (FT-IR) spectra of styli before and after demineralization clearly indicates the presence of phosphate (*SI Appendix*, Fig. S4), and phosphorous maps clearly show the colocation of iron and phosphorous in the stylus (see below).

It thus seems likely that the biomineral in the stylus is an iron(III) phosphate that is structurally distinct from AFP. The primary difference between this phosphate in the stylus and AFP in the core is the higher quadrupole splitting in the former, an indication that the octahedral coordination geometry of iron is distorted to a greater degree (Fig. 2*D*). We expect that this is correlated to an increase in average Fe-O bond length (25). Such an increase could result for example from the introduction of

Downloaded at Universiteit Gent on June 10, 2021

μ-hydroxo bridges. The stylus indeed has an orange-brown hue compared to the yellowish core, consistent with a larger fraction of μ-hydroxo oligomers (*SI Appendix*, Fig. S11) (31). As a consequence, we expect that the composition, in particular the relative amount of iron and phosphate, changes.

We therefore used scanning electron microscopy (SEM) in conjunction with energy dispersive X-ray spectroscopy (SEM-EDS) to determine the distribution of iron and phosphorous (Fig. 3). Inspection reveals that the tooth core has high levels of Fe (Fig. 3 *B* and *F*) and P (Fig. 3 *C* and *G*) that are fairly homogeneously distributed, with a Fe/P ratio close to 1 (Fig. 3 *D* and *H*), as would be expected for AFP (32). The stylus on the other hand is strongly graded, with the highest concentrations of Fe and P in the area just beneath the cusp and surrounding the end of the stylus canal, similar to a prior report (22). Note that gradients in the Fe/P ratio maps appear less smooth and pixel-to-pixel variation higher than they likely are in the stylus because of the significant downsampling necessary for the calculation of Fe/P ratios with a relative uncertainty on the order of 10%. Strikingly, the Fe/P ratio in the stylus is significantly higher, up to 1.5 on the posterior side and closer to 1.4 on the anterior side of the upper stylus (Fig. 3 *D* and *H*) Taken together, these observations support the hypothesis that the stylus mineral is a hydrated ferric (oxy/hydroxy)phosphate.

The final piece of evidence that allowed us to identify the stylus mineral comes from an analysis of the X-ray absorption near edge structure using an X-ray microprobe (Micro X-ray Near Edge Structure [μ-XANES]; refer to *SI Appendix*, Fig. S2 for spot positions). While pre-edge features in spectra of core and stylus are similar in that they are fairly broad, as expected for amorphous compounds, they also display distinct features (Fig. 4*A* and *SI Appendix*, Fig. S15). Spectra of the core and synthetic AFP both show a rather weak shoulder at low energy and a slightly more pronounced one at higher energy relative to the main feature, consistent with literature data (27, 32). In contrast, the main pre-edge feature in the stylus shows the onset of splitting. Spectral deconvolution indicates that this is due to a much-increased intensity of the component at higher energy (7,113.9 eV, Fig. 4*A* and *SI Appendix*, Tables S4–S6). In oxidic iron(III) compounds, these are linked μ-oxo or μ-hydroxo bridges connecting FeO_6 octahedra (33). We note that the third component at lower energy (7,111.0 eV) also increases in intensity relative to the most intense component at intermediate energy (7,112.6 eV). This may be a consequence of a small amount of beam-induced reduction to Fe(II).

The characteristic features of the pre-edge are consistent with those of santabarbaraite (SBB) $[Fe_3(PO_4)_2(OH)_3 \cdot 5\ H_2O]$, a rare amorphous ferric hydroxyphosphate with an Fe K-edge XANES spectrum strikingly close to that of the stylus (*SI Appendix*, Fig. S16 and Table S7) (34). Unlike in AFP, bridging between corner-sharing octahedra in SBB is thought to involve both μ-hydroxo bridges and phosphates in which both octahedra share the same oxygen (μ-phosphato-κO coordination, Fig. 4*F*) (35). The latter motif is known to increase Fe-O bond lengths and almost certainly contributes to the longer average value in SBB (2.04 Å) compared to that in AFP (1.98 Å) (25, 32, 34). This increase is fully consistent with the increase in quadrupole splitting we observed by SMS. Experimental Fe/P values for geological SBB are in the range of 1.3 to 1.4 (34) (i.e., a little below the nominal value of 1.5 but similar to our observations for the stylus). We are therefore confident that the mineral found in the stylus is SBB. The nonstoichiometric composition may be a feature of the mineral, but some AFP may also be present. For a

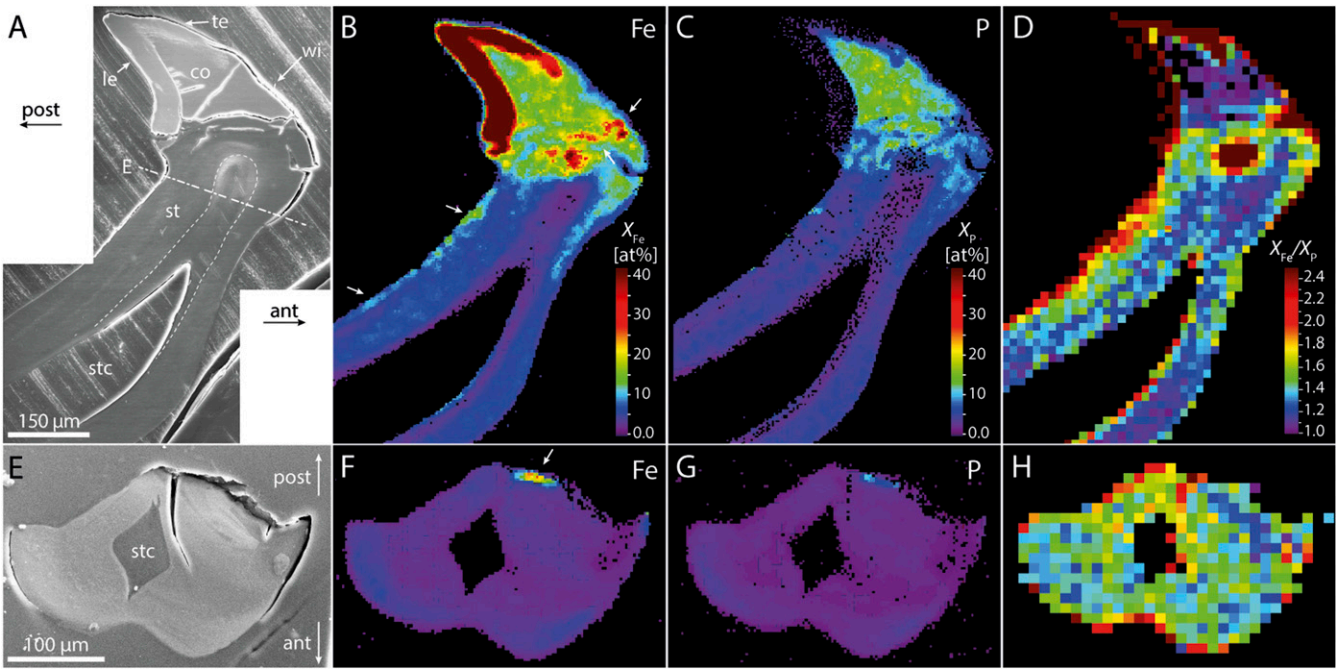

Fig. 3. Distribution of iron and phosphorous in the major lateral teeth of *C. stelleri*. (*A–D*) Longitudinal section of the tooth and upper stylus. (*E–H*) Transverse section of the upper stylus oriented approximately as shown by the dash-dotted line in *A*. SEM images using secondary electron contrast (*A* and *E*). Stylus canal (stc); core (*C*), window (wi), anterior (ant) and posterior (post) directions; leading edge (le); and trailing edge (te). Note that the stylus canal in this slightly oblique longitudinal section extends further toward the tooth head in the area indicated by the dashed line in *A*. SEM-EDS elemental maps report the mole fraction of Fe (*B* and *F*), P (*C* and *G*), and the Fe/P ratio (*D* and *H*). Mole fractions were calculated considering only the abundance of C, O, Fe, and P. Note that mole fractions of Fe near cracks in the tooth or between the tooth and the resin are over reported (white arrowheads). Maps were downsampled to ensure that the relative uncertainty of the Fe/P ratio is less than 10%, based on propagated uncertainties using counting statistics.

Downloaded at Universiteit Gent on June 10, 2021

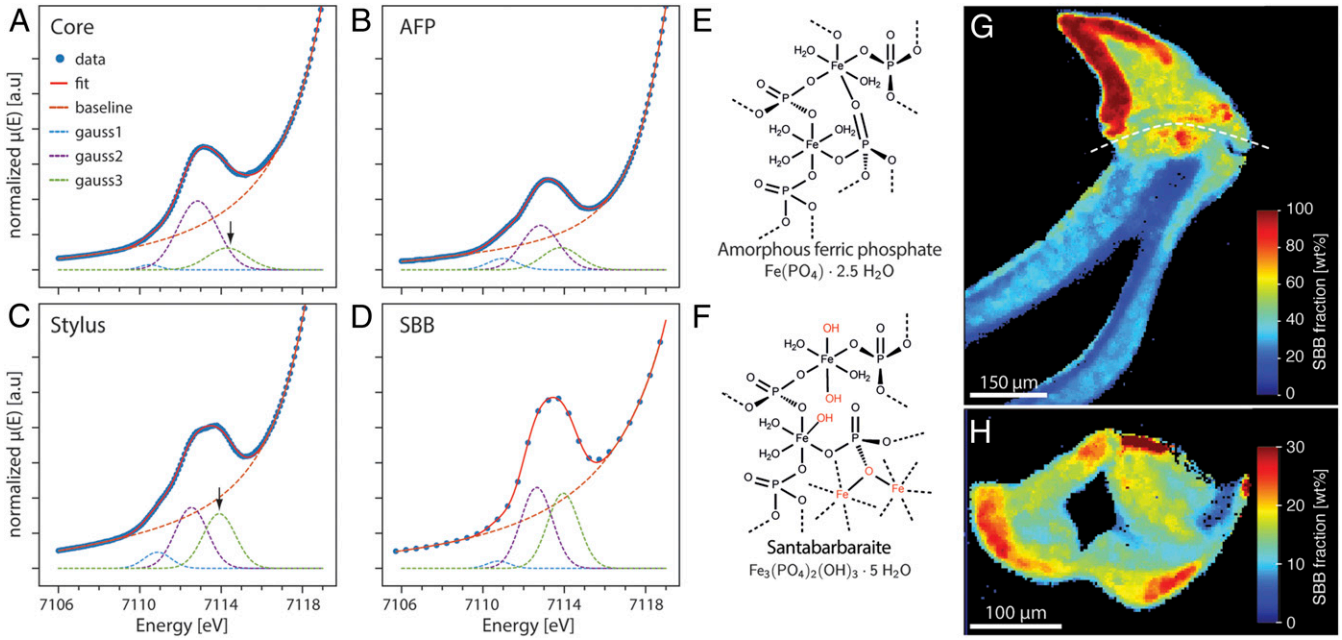

Fig. 4. Spectral characteristics and structure models of amorphous biominerals in the stylus of *C. stelleri*. (*A*) Plot of the pre-edge region of Fe K-edge XANES spectra of tooth core (*A*), synthetic AFP (*B*), upper stylus (*C*), and geological SBB (*D*). Experimental data points (closed blue circles), and a fitted model (red line) comprised of four components (dashed lines). Note large increase in intensity of the third Gaussian component at 7114 eV from the core to the stylus (arrow). For fitting range, constrains, and fitted parameters, refer to *SI Appendix*, Tables S5–S7. For residuals, refer to *SI Appendix*, Fig. S15. (*E*) Structural model for AFP in the core. (*F*) Structural model for SBB in the stylus. The atoms highlighted red mark structural elements that are unique to SBB. (*G* and *H*) False-colored map of estimate of the weight fraction of SBB in the stylus composite in a longitudinal (*G*) and transverse (*H*) section. Note that estimates are valid only for regions where the Fe/P ratio (Fig. 3 *D* and *H*) is in the range 1.2 to 1.7, roughly below the white dashed line in *G*.

more detailed analysis, phase mapping by linear combination analysis of μ-XANES spectra will be required.

Having identified SBB as the mineral phase in the stylus, we can estimate its mass (Fig. 4 *G* and *H*) and volume fraction (*SI Appendix*, Fig. S6) based on the mole fraction of iron. Inspection of the longitudinal section reveals a decreasing mineral content from the top of the stylus (55 wt%, 45 vol%) down the posterior and anterior side (20 wt%, 15 vol%). The anterior side shows a slightly increased mineral content, especially close to the top. The transverse section shows a decrease of mineral content from the outer stylus surface (25 wt%, 15 vol%) to the interior surface of the stylus canal (10 wt%, 5 vol%). Notably, the degree of mineralization is much higher than one would anticipate based on the abundance of iron alone. This is because the mole fraction of Fe in SBB is less than one-quarter of that in magnetite. Consequently, O and P contribute almost 70% of the mineral mass, compared to 28% for O in magnetite. Replacement of iron with lower mass atoms in the mineral component might be part of a strategy to increase the specific strength of the stylus composite and is likely the reason why the stylus has been described as an unmineralized tissue previously.

While use of amorphous mineral precursors is fairly widespread in biology, systems in which an amorphous rather than a crystalline mineral is used as permanent structural component in mature mineralized tissue are fairly rare outside the silicifying organisms. Even more rare is the presence of multiple amorphous phases in the same organism. A famous example is the calcium carbonate system in which both polymorphism and polyamorphism has been observed in the same organism; however, the polyamorphs are transient (36). To the best of our knowledge, the parallel use of two persistent polyamorphs, here AFP and SBB, in well-defined microstructural domains is unprecedented and underlines the very high level of control that the chiton exerts over mineralization. Note that we use the term polyamorphisms here loosely to describe amorphous materials that differ not only in structure, but also to some degree in composition.

Given that differentiating between AFP and SBB required sophisticated analytical techniques, it is possible that the latter has been overlooked in other species. Presence of ferric iron and phosphate is clearly a necessity, and so, the closest suspects are species in which AFP has been identified but SBB not explicitly ruled out. Within the mollusks, these include the radula tooth complex of chitons and limpets other than *C. stelleri* and the gizzard plates of certain gastropods (37), in echinoderms, mesodermal granules in sea cucumbers, deposits in the gut of heart urchins (37, 38), in bristleworms, sternal shields, and tube linings (37). Casting a wider net, consider that small amounts of iron are found in apatitic tissues such as bone, dentin, and enamel (3 to 138 ppm) (39). Both Fe^{2+} and Fe^{3+} strongly favor the precipitation of amorphous calcium phosphate (40). Due to low solubility in the apatite lattice, segregation of iron may lead to greatly elevated concentrations at interfaces, which in turn may lead to precipitation of iron-rich phases. In pigmented dental enamel, for example, we identified an amorphous intergranular phase comprised of ferrihydrite and Ca-substituted AFP that greatly impacts both the chemical and mechanical behavior of enamel (41). Given we know very little about the formation of pigmented enamel, it is conceivable that SBB might form alongside AFP or in its place in some species. Much higher amounts of iron, up to 7.1 wt%, have been reported in the nominally apatitic tooth core of the *Chitonidae*, greatly increasing the likelihood and expected abundance SBB and/or AFP (42).

Further afield, iron-depositing organisms have been identified among the cyanobacteria, green and golden algae, euglenoids, and foraminifera (43, 44). Similar to "iron bacteria," such as

Downloaded at Universiteit Gent on June 10, 2021

Leptothrix, and other species that are often present in complex, ferric iron–encrusted biofilms, it is likely that mineralization is biologically induced rather than controlled (45). For instance, there are examples in which iron-oxidizing bacteria in phosphate-rich environments progressively transform ferrous vivianite ($Fe_3[PO_4]_2{\cdot}8H_2O$), by indirect oxidation into an amorphous ferric phase. As part of this process, the Fe/P ratio increases from 1.3 to 3, such that SBB could be formed at least transiently (46).

Returning to processes under genetic control, ferric iron and phosphate intersect in almost all life in the ferritin superfamily of proteins. Multimeric nanocages that can hold hundreds to thousands of ions, ferritins ensure that iron is bioavailable in a soluble, nontoxic form. While in animals the Fe/P ratio is high (~8 to 10) and the dominant iron mineral is ferrihydrite, in bacterial ferritins and to a lesser degree in plants, the Fe/P ratio is in a range that is consistent with SBB being present (e.g., *Azotobacter vinelanddii*: Fe/P = 1.1 to 1.5; *Pisum sativum*: Fe/P = 2.8) (47, 48). A second example of a tightly controlled process is the formation of magnetic nanoparticles in magnetotactic bacteria in which SBB might occur as part of a phosphate-enriched precursor phase (49). Finally, if we relax our criterion that both ferric iron and phosphate need to be documented, we note that there are examples of chitinous insect cuticle that may be strengthened with iron (50). While no counterion, much less a mineral phase has yet been identified, we think it is likely that the combination of techniques we used herein would help clarify whether these tissues are composites similar to the chiton stylus.

The stylus is a highly graded composite composed of a soft chitin matrix and SBB as a hard, inorganic filler. For the properties of this composite, the dispersion, size, and shape of inorganic particles and the strength of the interface are of central importance. We therefore compared fracture surfaces of native and demineralized styli using SEM. Those of native styli show features typical for brittle fracture with strong matrix/particle interaction, namely, a rough surface with no indications for fiber pull-out (Fig. 5*A* and *SI Appendix*, Fig. S5*B*) (53). In contrast, fracture surfaces of demineralized styli clearly show the fibrous nature of the chitin matrix (*SI Appendix*, Fig. S5 *C* and *D*), with fiber bundles ranging from 30 nm to 500 nm in size and individual fibrils with diameters of 10 to 20 nm. A closer look at demineralized samples revealed that there are small pores, about 10 nm in width, often arranged in stacks parallel to the fiber direction (Fig. 5*B* and *SI Appendix*, Fig. S5 *C* and *D*). This feature is unique to demineralized samples and may correspond to the space left behind as the mineral dissolved.

Transmission electron microscopy (TEM) images of thin sections of the upper mineralized stylus that were recorded using bright-field (BF) contrast reveal periodic contrast modulation parallel to the antidiagonal consistent with chitin fibrils preferentially aligned in this direction (Fig. 5*C* and *SI Appendix*, Fig. S7). Fast Fourier transform analysis of TEM-BF images indicates a dominant if broad distribution of wavelengths centered on 15.3 nm (*SI Appendix*, Fig. S7*E*) in the direction of the antidiagonal. This likely corresponds to a center-to-center distance between mineral particles separated by a fibril. Additional characteristic length scales include 7.6, 4.1, and 3.5 nm. Based on the distribution of spatial frequencies (*SI Appendix*, Fig. S7*E*) and contrast variation in TEM images, we estimate that the fibril diameter is 4 to 5 nm, similar to that described for limpet teeth (54). Images further reveal numerous small features that appear dark, consistent with dense mineral particles embedded in an organic matrix (Fig. 5*D* and *SI Appendix*, Fig. S8). Selected area electron diffraction (*SI Appendix*, Fig. S8 *W–Y*) only shows a diffuse band at approximate $(4.85\ \text{Å})^{-1}$, consistent with an amorphous mineral phase. However, we cannot rule out that α-chitin also contributes to this band. Images taken at higher resolution suffer from diminished contrast but reveal the presence of nanoparticles with a diameter of 3 to 11 nm (*SI Appendix*, Fig. S8*V*) embedded in the fibrous matrix. Given the small size of the mineral particles, the surface area between mineral and matrix is expected to be substantial (2.3 to 8.3 $m^2 \cdot g^{-1} \cdot vol\%^{-1}$); based on the fracture behavior, it is also quite strong.

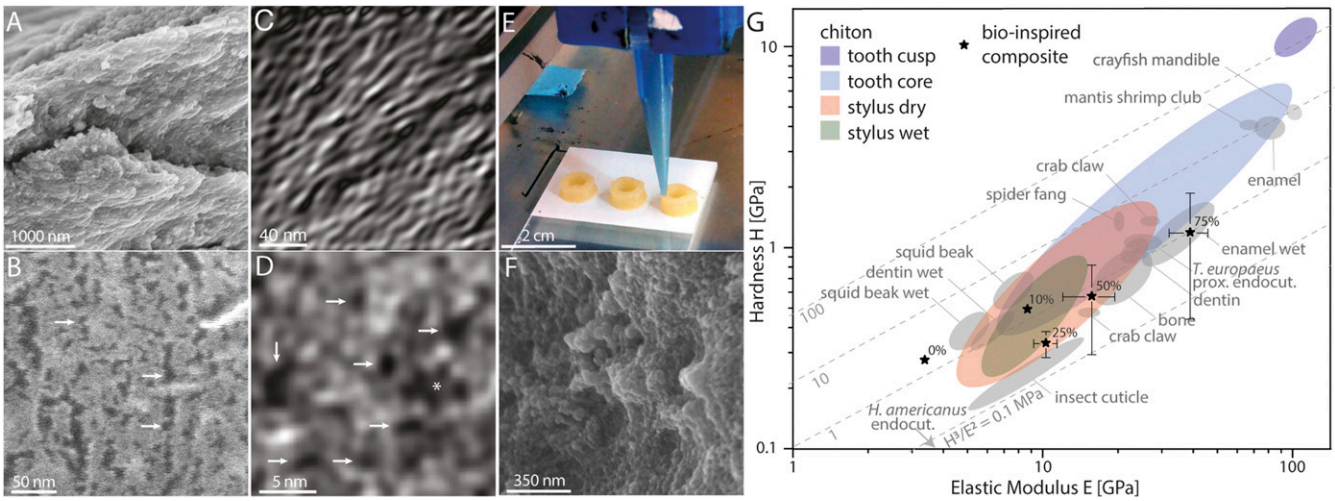

Fig. 5. Properties of the *C. stelleri* stylus and a bio-inspired synthetic composite. (*A* and *B*) SEM images of fracture surfaces of mineralized (*A*) and demineralized (*B*) stylus. Note the presence of small pores in the demineralized sample (white arrows). (*C* and *D*) Filtered TEM-BF images of a transverse thin section of the upper stylus. The predominant orientation of chitin fibrils parallel to the antidiagonal is revealed by a circular Butterworth filter (*C*) whereas a low-pass filter reveals mineral particles (D, white arrows). Note that because of the section thickness, particles that appear to cluster (asterisk) may not actually be close to each other. Please refer to *SI Appendix*, Figs. S7 and S8 for unfiltered images, filter design, and spectral analysis. (*E*) 3D printing of bio-inspired AFP–chitosan composites. (*F*) SEM image of a fracture surface of the composite (75 wt% mineral) displays microstructure similar to that of the stylus (*A*). (*G*) Ashby plot of hardness versus elastic modulus of chiton radula tooth cusp (purple, blue) and stylus (red, green); a sampling of biomineralized tissues (gray) (3, 51, 52); and bio-inspired composites with 0 to 75 wt% nominal mineral content (black stars). Unless otherwise indicated, data refer to dry samples. Error bars indicate one SD and are too small to be visible for samples with up to 10wt% mineral. The dashed diagonal lines indicate a metric for wear resistance H^3/E^2.

Downloaded at Universiteit Gent on June 10, 2021

The nano-architecture of the chiton stylus, with a fine dispersion of mineral nanoparticles in the matrix, is similar to certain arthropod cuticles. The endocuticle of the lobster *Homarus americanus*, for instance, is a fibrous matrix with a characteristic chitin fibrils diameter of 3 to 5 nm that is reinforced by spherical amorphous calcium carbonate (ACC) particles with a 20- to 50-nm diameter (55, 56). In the proximal endocuticle of the isopod *Tylos europaeus*, a 4-nm-thick ACC layer coats protein–chitin fibrils with 6- to 8-nm diameter (57). The cuticle of the isopod is significantly harder (H = 1.0 to 1.3 GPa versus 30 to 55 MPa) and stiffer (E = 24 to 29 GPa versus 3 to 5 GPa) than that of the lobster (51, 52). We find, using nanoindentation, that the stylus of *C. stelleri* not only has a much wider range than either of these examples but also reaches much higher hardness values (Fig. 5*G* and *SI Appendix*, Figs. S17–S20). Specifically, hardness ranges over almost an order of magnitude (H = 0.2 to 1.8 GPa, Fig. 5*G* and *SI Appendix*, Fig. S19) and reaches a maximum almost 40% higher than that of *T. europaeus*. While the variation of the reduced elastic modulus is less dramatic (E = 7 to 30 GPa, Fig. 5*G* and *SI Appendix*, Fig. S19) and has a maximum similar to that of *T. europaeus*, the relative range is more than 10 times as high (~375% versus 20%).

Mechanical property maps reveal that values for the core of the upper stylus and especially the walls of the stylus canal cluster at the softer end of the range, whereas the outer part is stiffer and harder (*SI Appendix*, Fig. S18). This has recently been shown also and in great detail by Pohl and coworkers (22). Notably, the range of mechanical properties of stylus and the tooth core show some overlap, with the core extending the hardness range to 3.6 GPa and the reduced elastic modulus to 86 GPa, values that are comparable to vertebrate enamel (Fig. 5*G*), even outperforming it in its wear resistance H^3/E^2 (58).

Given the impressive performance of SBB and AFP-based composites in the chiton tooth, we set out to apply some of the design principles at a larger scale. In the chiton, the organic tooth matrix is deposited by odontoblasts with excellent control over which and how much mineral is formed where and when. This is quite difficult to reproduce without a much deeper understanding of the biological mechanisms at play and may be challenging to scale up due to inefficient transport of mineral precursors by diffusion. However, we hypothesized that larger structures might be produced by additive manufacturing techniques, using inks in which amorphous nanoparticles would form in situ. As a base polymer, we chose chitosan acetate, a highly charged, cationic polysaccharide similar to partially deacetylated chitin. Highly viscous solutions (10 wt% in water) were mixed with aqueous solutions of ferric acetate and diammonium hydrogen phosphate using a high-efficiency mixer. Inks could then be 3D printed into objects that held their own shape (Fig. 5*E*). Water and excess ammonium acetate were removed by drying. Composites with nominal (dry) mineral weight fractions between 10 wt% and 75 wt% were produced in this way.

Under these conditions, we expect AFP rather than SBB to form; there is no known synthesis for the latter. We confirmed the presence of AFP in the final composites using FT-IR (*SI Appendix*, Fig. S4), XANES (*SI Appendix*, Fig. S15), and TEM selected area diffraction (*SI Appendix*, Fig. S9). While fracture surfaces appeared similar to those of mineralized stylus (Fig. 5*F* cf. Fig. 5*A*) and the tooth core (21), TEM indicated that AFP precipitates at 30- to 50-nm diameter (*SI Appendix*, Fig. S9) were substantially larger than AFP particles in the core (17) and SBB particles in the stylus.

Nano-mechanical testing of composites revealed that over the range of the nominal mineral content, they performed similar to the stylus (Fig. 5*G* and *SI Appendix*, Table S8). While elastic moduli covered a comparable range (E = 9 to 39 GPa), hardness values were slightly lower (H = 0.3 to 1.2 GPa) and did not increase as strongly with increasing mineral fraction. We also note that at similar mineral loading, the synthetic composites are not quite as hard and stiff as the tooth core. This is likely due to a combination of factors, including the larger particle size and the absence of crystalline chitin fibers. Finally, the variance for higher loadings is high, indicating that particles are not as well dispersed as in the stylus tissue. While there is clearly room for improvement, it is worth pointing out that the chitosan/AFP composite at 75 wt% mineral loading compares favorably in terms of modulus with, for example, dental composites with similar mineral content (59, 60).

Conclusion

In conclusion, we find definite proof that the stylus of the major lateral tooth of *C. stelleri* is a mineralized tissue. We identify the mineral phase as SBB that was not previously known as a biogenic mineral. This makes *C. stelleri* the only known organism that uses persistent polyamorphs in close proximity in the same mineralized tissue. SBB is very finely dispersed in the stylus, with typical particle diameters in the range from 3 to 11 nm. Its distribution in the stylus is highly graded, indicating that tight biological controls are in place. An analysis of nano-mechanical properties of the upper stylus and core reveals that chitin-based composites using SBB and AFP span a very large, overlapping range of hardness and elastic modulus. This allows the chiton to create composites with complexly and continuously graded mechanical properties. Based on these insights, we designed bio-inspired inks for 3D printing of composites in which AFP nanoparticles form in situ. Mechanical properties of composites approach those of the stylus, indicating that we captured some but not all design parameters. However, we anticipate that further improvements will be straightforward. Inks and composites are comprised of biodegradable and nontoxic components, can be processed at room temperature in aqueous solvents, and perform similar or better than, for example, dental composites with similar filler loading. Given the emergence of functional properties from mechanical gradients, we anticipate that this approach will be particularly valuable for additive manufacturing for soft robotics.

Materials and Methods

Animal Specimens. Live *C. stelleri* (150 to 290 mm in length; 150 to 650 g in weight) were obtained from a commercial supplier (Monterey Abalone Company). Specimens were collected in the Eastern Pacific Ocean (on/off the coast of Monterey, CA) and shipped overnight, packed live in ice and protected by plastic foam. Chitons do not move while shipping at such low temperatures. After arrival, animals were maintained in a marine life support system in artificial seawater at 12 °C and fed with kelp until use.

Dissection. Animals were killed by a scalpel cut along the foot. The radula was removed surgically, washed with jet of deionized (DI) water to remove the epithelial tissue (61), dehydrated by placement in aqueous ethanol of increasing concentration (10%, 25%, 50%, and 75% [vol/vol]), and dried in air. In this study, mature teeth only were used from the first eight rows of the anterior end of the radula.

Removal of Tooth Heads. For some samples, heads of the major lateral teeth were removed by placing a microscope slide on top of the dehydrated radula and applying pressure. This results in fracture close to the interface between head and stylus. Loose heads were collected using a rare-earth magnet.

Demineralization. Tooth heads were removed from a dehydrated piece comprised of the anterior two-thirds of the radula as described above. The radula was then placed into 300 mL of a solution containing citric acid (500 mM) and ascorbic acid (500 mM) in DI water. Demineralization was performed over 72 h at room temperature (RT) with gentle agitation on a shaker (Polymax 1040,

Downloaded at Universiteit Gent on June 10, 2021

Heidolph) and exchanging the solution 24 h. The radula was then washed with DI water (3 × 300 mL) and dried at 37 °C for 36 h in an incubator.

Isolation of Styli. Individual styli were then separated from mineralized radula membranes after dehydration and removal of tooth heads or from demineralized and dried radula membranes using fine-tipped tweezers under a dissection microscope (Wild MZ3, Leica Microsystems).

Fracture Surfaces and Sections. Styli were extracted from mineralized or demineralized radula membranes as previously described. Fracture surfaces were prepared using a diamond scribe. For transverse sections, individual styli were embedded in epoxy and cured overnight in air at RT. The resin block was trimmed with a razor blade. The block face was then planed using an ultramicrotome (UC7, Leica) equipped with a glass knife until the surface of the transverse section was exposed.

For longitudinal sections, a piece of radula with several rows of teeth was embedded in epoxy and cured overnight in air at RT. Sections 100 to 200 μm in thickness were prepared using a slow-speed diamond saw (Isomet, Buehler). Sections were fixed to a glass coverslip with cyanoacrylate glue and polished using diamond polishing suspensions (3 μm and 1 μm) on Trimed cloth followed by silica polishing suspension (40 nm) on Chemomet cloth.

Nanoindentation. Indentation experiments were performed at ambient temperature and 40% humidity (longitudinal) or 95% humidity (transverse) using a nano-mechanical testing system (TI 950 Triboindenter, Hysitron). Load-controlled indents were performed at 1,400 μN using a Berkovich indenter tip. The load function consisted of a 5-s loading step, 2-s hold, and 5-s unloading step. Hardness and elastic modulus were calculated from the unloading curve of each indent using the method of Oliver and Pharr (62).

TEM. Thin sections (80 to 120 nm) were prepared from resin blocks prepared as described for transverse sections but using an ultramicrotome (Leica UC7, Wetzlar) equipped with a diamond knife (45° Diatome). Sections were floated on a saturated solution of AFP (32) and collected immediately using a formvar-coated slot grid (0.4 × 2 mm, Ted Pella). Approximately 120-nm-thick sections were imaged on a JEOL ARM 300F equipped with a cold-field emission gun and operated at an accelerating voltage of 300 keV. Images were acquired on a Gatan OneView-IS camera in conventional TEM mode. To minimize beam-induced damage, we used a total emission current of 10 μA, which resulted in an electron dose rate of 0.09 pA · cm^{-2} (56 e$^-$ Å^{-2} · s^{-1}). We ensured that the total electron dose was < 25 e$^-$ · Å^{-2} per image. Additionally, we confirmed that such image acquisitions did not result in observable radiation damage displayed by contrast fluctuations after visual inspection of the imaged area. Images were analyzed in Gatan Digital Micrograph Suite 3.0 (GMS; Gatan). Filtering in the frequency domain was performed in MATLAB and is described in more detail in *SI Appendix*.

SEM and SEM-EDS. Sections and mechanically fractured samples were dried for 24 h at RT and a pressure of 8 mbar. They were affixed with carbon tape to an aluminum stub and coated with a film of gold or aluminum (20-nm thickness, Denton III Desk sputter coater). SEM images were recorded on a Hitachi SU8030 operated at 10 to 15 keV, a working distance of 2 mm, and using an upper secondary electron detector or a backscatter detector. The contrast of the SEM pictures was adjusted with ImageJ (63).

SEM-EDS was performed at 30 keV and a working distance of 15 mm, using an Oxford AZtec X-max 80 silicon drift detector EDS detector in Quant map mode. Maps with a size of 512 pixels by 384 pixels (0.78-μm pixel pitch) were recorded with a dwell time of 30 μs for a total of 15 to 30 min. Data were analyzed and quantified with the Aztec software with the help of quantification reference standards. The data are not absolutely quantified but quantitative in respect to the other elements detected ("normalized").

For reproduction, elemental maps were binned (4 × 4) and then filtered with a median filter (2 pixel radius) using ImageJ (63) to reduce noise while maintaining edges. The Fe/P ratio maps were obtained from binned (16 × 16), unfiltered elemental maps. We estimate an average uncertainty of 10% based upon counting statistics.

To estimate the SBB mass fraction, we assumed the following:

$$X_C = 1 - X_{Fe} - X_P = 1 - X_{Fe} - \frac{2X_{Fe}}{3}$$

and

$$w_{SBB} = \frac{8X_{Fe}M_{SBB}}{3M_{SBB} + X_{Fe}(8M_{SBB} - 5M_{chitin})}$$

where X_{Fe}, X_P, and X_C are mole fractions determined by EDS, w_{SBB} is the mass fraction of SBB in the stylus, and M_{SBB} and M_{chitin} are the molecular weights of SBB (466.57 g · mol^{-1}) and the chitin repeat unit (203.1 g · mol^{-1}). The corresponding volume fraction was calculated based on the density of α-chitin (1.46 g · cm^{-3}) (64) and SBB (2.42 g · cm^{-3}) (34).

μ-XANES. X-ray absorption spectromicroscopy at the iron K-edge was performed at the Geo Soil Enviro Consortium for Advanced Radiation Sources X-ray microprobe beamline (13-ID-E) at the Advanced Photon Source (APS), Argonne National Laboratory (Argonne, IL) (65). A longitudinal section of a mature tooth, including the upper stylus, was prepared as described above. Synthetic AFP (32) and 75 wt% AFP ink (ESI) were used as reference compounds. Powdered reference samples were spread uniformly on adhesive tape (Scotch Magic Tape, 3M). Multiple layers (3–5) of tape were then stacked to optimize X-ray absorption.

Using a beam focused to 1 × 1 μm^2, X-ray fluorescence maps were recorded to determine regions of interest for subsequent μ-XANES. XANES spectra were collected in fluorescence mode using a four-element, silicon drift diode detector array (Vortex-ME4, Hitachi High-Technologies Science America, Inc.), with pulse-processing provided by an Xspress 3 digital X-ray processor system (Quantum Detectors). The incident beam energy was scanned in 6 eV steps from 7,012 to 7,102 eV, in 0.1 eV steps from 7,102 to 7,132 eV, and in 1.5 eV steps from 7,132 to 7,740 eV, with a dwell time of 0.5 s. All spectra were recorded under a helium atmosphere. Under these conditions, single scans resulted in spectra of sufficient quality for analysis. Spectra were calibrated to the inflection point of zero-valent Fe foil (E_0 = 7,110.75 eV) (66) and were normalized to the incident beam intensity (I_0) measured in a helium-filled, 200-mm-long ion chamber just upstream of the Kirkpatrick–Baez mirror optics. All XANES data were corrected for detector dead time, self-absorption, and normalized with Athena or X-raylarch (67). To improve signal-to-noise, normalized spectra of geological SBB were downsampled by averaging over blocks of three data points on the energy and intensity axes.

Pre-edge features were isolated by fitting and then subtracting a baseline consisting of a linear and a Lorentzian function to the main edge:

$$\hat{I}(E) = \hat{O} + \hat{M}E + \frac{\hat{B}\hat{s}}{\pi}\left[\left(E - \hat{\mu}_{edge}\right)^2 + \hat{s}^2\right]^{-1}$$

where $\hat{I}$ is the fitted intensity and energy E is the independent variable. $\hat{B}$, $\hat{s}$, $\hat{M}$, and $\hat{\mu}_{edge}$ locally define the absorption edge together with offset $\hat{O}$. This first fit was performed excluding an energy window in which pre-edge features have substantial intensity (*SI Appendix*, Table S4). The pre-edge (i.e., the residual from the first step) was then fit with three Gaussian components, using the X-raylarch (68) and lmfit (69) packages for Python, with the following model:

$$\hat{I}(E) - \hat{O} - \hat{M}E - \frac{\hat{B}\hat{s}}{\pi}\left[\left(E - \hat{\mu}_{edge}\right)^2 + \hat{s}^2\right]^{-1} = \sum_{i=1}^{3} A_i e^{-\frac{(E-\hat{\mu}_i)^2}{2\hat{\sigma}_i^2}}$$

where $\hat{A}_i$ is the prefactor, $\hat{\mu}_i$ the mean, and $\hat{\sigma}_i$ the SD of the ith Gaussian component. The FWHM can be calculated as $\hat{w}_i = 2\hat{\sigma}_i\sqrt{2\ln 2}$. Gaussian components 2 and 3 represent 1s → 3d transitions and were fit with the same $\hat{\sigma}_2 = \hat{\sigma}_3$. Gaussian component 1 does not arise from a 1s → 3d transition and was fit with an independent SD (70). For additional constraints, see *SI Appendix*, Table S5, for fit parameters, see *SI Appendix*, Table S6, and for graphs of the fitted components and overall residual, see *SI Appendix*, Fig. S15.

To determine the relative contribution of the components to the pre-edge, we used the analytical solution

$$\int_{-\infty}^{\infty} \hat{A} e^{-\frac{(E-\hat{\mu})^2}{2\hat{\sigma}^2}} = \frac{\hat{A}\hat{\sigma}}{2}\sqrt{\frac{\pi}{\ln 2}}$$

for the improper integral of the Gaussian components. This allows writing the area fraction of the ith component as

$$f_{A,i} = \frac{\hat{A}_i\hat{w}_i}{\sum_{i=1}^{3}\hat{A}_i\hat{w}_i} = \frac{\hat{A}_i\hat{\sigma}_i}{\sum_{i=1}^{3}\hat{A}_i\hat{\sigma}_i}$$

Synchrotron X-ray computed microtomography was performed on beamline 5-BM-C (DuPont, Northwestern, Dow Collaborative Access Team [DND-CAT]) at the APS, Argonne National Laboratory (Argonne, IL). A radula tooth

Downloaded at Universiteit Gent on June 10, 2021

fragment including the head and upper stylus was removed from a freshly dissected and dehydrated radula using tweezers and attached to a glass capillary pulled to approximately 10-μm tip diameter, using cyanoacrylate glue. The following collection parameters were used: 20 keV monochromatic X-rays, 1.0-s integration time per projection, and 1,200 projections over 180° (0.15° increments). Radiographs were collected with a 1,300 × 1,240–pixel, 24-mm Roper Scientific (Photometrics) charge-coupled device detector after X-ray–to–optical conversion with a CDW phosphor and magnification by a 4× lens. A dark frame was collected at the beginning of the scan. After every fifth projection (~5 s), a flat-field measurement was taken to normalize patterns and account for intensity drifts of the beam source. Reconstructions were performed on site using a six-node Linux cluster implementing a filtered back-projection algorithm with a Shepp–Logan kernel. The final isometric voxel edge length was 2.4 μm. The 3D visualization and rendering of the data were performed using the Amira software package (Thermo Fisher Scientific).

SMS. SMS was performed at the beamline 3-ID-B at the APS, Argonne National Laboratory using a beam focused to 10 × 15 μm^2 (for details of the experimental setup, please refer to ref. 24). The incident beam energy was held within ± 0.2 meV of the resonance frequency of ^{57}Fe (14.41 keV). The Mößbauer effect was excited with the storage ring operating in 24-bunch mode, resulting in a separation of bunches by 153.4 ns. The time-dependent intensity of nuclear forward-scattered (NFS) photons was recorded by an avalanche photodiode detector in the window from 23 to 120 ns.

For SMS imaging, longitudinal sections (thickness = 150 μm) prepared as described above were mounted on sapphire discs using cyanoacrylate glue. The sample was scanned through the beam with a step size of 15 μm in the x- and y-directions and a dwell time of 4 s. The resonance intensity was determined by integrating over NFS intensity from 23 to 120 ns (total iron, Fig. 2*A*) or from 55 to 67 ns (magnetite selective, Fig. 2*B*). Resonance intensity maps were used to identify regions of interest for point spectra. For display, maps were smoothed using the MATLAB (Mathworks) imgaussfilt function with an SD of 1 and rendered as a filled contour map.

The delayed count rate varied between three (stylus) and 33 (tip of cusp) photons · s^{-1}. Spectra (*SI Appendix*, Figs. S12 and S14) were taken for a duration of 0.5 to 5 h. Hyperfine parameters (*SI Appendix*, Tables S2 and S3) were extracted using CONUSS (71). Briefly, time domain spectra were fitted to obtain the quadrupole splitting (Δ), magnetic hyperfine field (*B*), and isomer shift (δ) of the sample. Velocity domain spectra were then simulated based upon these parameters.

Additive Manufacturing. The 3D printing was conducted on a System 30M (Hyrel 3D) that was equipped with an SDS-10 extruder head fitted with a disposable syringe and a disposable nozzle. Inks were prepared using an ARE-310 planetary centrifugal mixer (Thinky USA, Inc). For ink preparation, please see "Synthetic Procedures" in ESI). The stage movement speed was adjusted depending on the viscosity of the ink (3 to 10 mm · s^{-1}), with slower speeds used for more viscous inks. The tip-to-substrate distance was ~200 μm. Frosted microscope slides were used as substrates. Printed objects were dried in a fume hood under a gentle stream of air for 7 d at RT.

Preparation of Inks for Additive Manufacturing. We chose chitosan rather than chitin as the organic component for the ink because of its solubility and ease of processing. Chitosan is derived from chitin, the second-most abundant biopolymer, by deacetylation of the amino group and is biocompatible, biodegradable, and nontoxic (72). For the mineral component, we chose AFP rather than santabarbaraite as a synthesis for the latter has not been described.

For most applications, structures significantly larger than chiton teeth are desirable. With increasing size, supplying mineral precursors through the surface becomes a limiting factor. We overcome this problem by premixing suitably stabilized mineral precursors in an organic hydrogel matrix. This requires a process compatible with high-viscosity media, such as centrifugal planetary mixing.

The choice of counterions for iron and phosphate building blocks was informed by 1) the need to prevent precipitation of iron oxides and 2) ease of removal of counterions after precipitation of AFP. We selected $Fe(OAc)_3$ as a suitable precursor because acetate ligands provide the necessary stability and therefore enable homogenous distribution of the precursor in the matrix. Given the high vapor pressure of ammonium acetate, we then chose $(NH_4)_2HPO_4$ as a phosphate source.

***Chitosan Acetate (ChitOAc)* (73).** A mixture of chitosan (5 g) and 90% (vol/vol) aqueous acetic acid (45 g) was sonicated for 24 h at RT. The resulting viscous liquid was poured into plastic Petri dishes and left to dry in a fume hood for 7 d at RT.

Solution A. Ferrous acetate (2,076 mg, 12 mmol) was dissolved in 90% (vol/vol) aqueous acetic acid (final volume 2 mL). Due to oxidation of Fe^{2+} by oxygen, the solution gradually turns from yellow/orange to deep red.

Solution B. A suspension $(NH_4)_2HPO_4$ (6 g, 45 mmol) in DI water (final volume: 10 mL) was stirred at 50 °C for 12 h to give transparent solution.

A mixture of chitosan acetate (500 mg) was sonicated in 20% (vol/vol) aqueous acetic acid (4.5 g) for 0.5 h at RT. The resulting, highly viscous solution was transferred into an ointment container (Umano UG, 12 mL, Thinky) and mixed for 20 min at 2,000 rpm using an ARE-310 planetary centrifugal mixer (Thinky USA, Inc). A total of 62 μL solution A (0.37 mmol, 21 mg iron) and 81 μL solution B (0.37 mmol, 34 mg phosphate) were added, and mixing continued for 20 min at 2,000 rpm. Air bubbles were removed by mixing at 500 rpm for 5 min. An aliquot corresponding to 20% (wt/wt) of the resulting mixture was removed and is referred to as ChiAc-$AFP_{10wt\%}$

To the remainder, 99 μL solution A (0.59 mmol, 33 mg iron) and 129 μL solution B (0.59 mmol, 56 mg phosphate) were added, and mixing continued for 20 min at 2,000 rpm. Air bubbles were removed by mixing at 500 rpm for 5 min. An aliquot corresponding to 25% (wt/wt) of the resulting mixture was removed and is referred to as ChiAc-$AFP_{25wt\%}$.

To the remainder, 222 μL solution A (1.3 mmol, 75 mg iron) and 290 μL solution B (1.3 mmol, 125 mg phosphate) were added, and mixing continued for 20 min at 2,000 rpm. Air bubbles were removed by mixing at 500 rpm for 5 min. An aliquot corresponding to 33% (wt/wt) of the resulting mixture was removed and is referred to as ChiAc-$AFP_{50wt\%}$.

To the remainder, 442 μL solution A (2.6 mmol, 149 mg iron) and 580 μL solution B (2.6 mmol, 250 mg phosphate) were added, and mixing continued for 20 min at 2,000 rpm. Air bubbles were removed by mixing at 500 rpm for 5 min. The resulting mixture is referred to as ChiAc-$AFP_{75wt\%}$.

Data Availability. Raw data were generated at several facilities, including the Advanced Photon Source, Argonne National Laboratory. Derived data that support the findings of this study are openly available on Github at https://github.com/bbimat-group/chiton_stylus. Raw data is available from the corresponding author D.J. on reasonable request.

ACKNOWLEDGMENTS. L.S. was supported by a research fellowship of the Deutsche Forschungsgemeinschaft (STE2689/1-1). This work was in part supported by the NSF (DMR-1508399 and DMR-1905982). R.F. was supported by an F31 fellowship from the NIH (NIH-DE026952). S.G.W. and M.C.H. acknowledge support from the Air Force Research Laboratory under Agreement FA8650-15-2-5518. The US Government is authorized to reproduce and distribute reprints for governmental purposes notwithstanding any copyright notation thereon. The views and conclusions contained herein are those of the authors and should not be interpreted as necessarily representing the official policies or endorsements, either expressed or implied, of the sponsors. This work made use of the following core facilities operated by Northwestern University: Materials Characterization and Imaging Facility (MatCI), BioCryo, Scanned Probe Imaging and Development (SPID), Northwestern University Atomic and Nanoscale Characterization Experimental Center (NUANCE), and Electron Probe Instrumentation Center (EPIC), which received support from the International Institute for Nanotechnology (IIN), the Keck Foundation, the State of Illinois, through the IIN; Integrated Molecular Structure Education and Research Center (IMSERC), and the Quantitative Bioelemental Imaging Center, which received support from the NASA Ames Research Center NNA06CB93G. MatCI, BioCryo, SPID, NUANCE, and EPIC were further supported by the Materials Research Science and Engineering Centers program (NSF DMR-1720139) at the Materials Research Center at Northwestern University. BioCryo, SPID, NUANCE, EPIC, and IMSERC were also supported by the Soft and Hybrid Nanotechnology Experimental Resource (NSF ECCS-1542205). It also made use of the CryoCluster equipment of BioCryo, which has received support from the Major Research Instrumentation program (NSF DMR-1229693). Portions of this work were performed at the DND-CAT located at Sector 5 of the APS. DND-CAT is supported by Northwestern University, The Dow Chemical Company, and DuPont de Nemours, Inc. Data were collected using an instrument funded by the NSF under Award 0960140. Portions of this work were performed at GeoSoilEnviroCARS (The University of Chicago, Sector 13), APS, Argonne National Laboratory. GeoSoilEnviroCARS is

CHEMISTRY

Downloaded at Universiteit Gent on June 10, 2021

supported by the NSF–Earth Sciences (EAR–1634415) and Department of Energy–GeoSciences (DE-FG02-94ER14466). This research used resources of the APS, a US Department of Energy Office of Science User Facility operated for the Department of Energy Office of Science by Argonne National Laboratory under Contract DE-AC02-06CH11357. We thank Oskar Lindenmayer and the Geosciences Collections of Museum Victoria, Melbourne, Australia, for geological SBB; Wenli Bi, Reiner Bleher, Robert Free, Michael Hu, Maya Kompella, Tony Lanzirotti, Matt Newville, Utthara Rameshabu, Eric Roth, Thomas Toellner, and Jiyong Zhao for technical support; and Tilman Grunewald, Friederike Hoeg, and Vivian Merk for discussion.

1. H. A. Lowenstam, Minerals formed by organisms. *Science* **211**, 1126–1131 (1981).
2. H. A. Lowenstam, S. Weiner, *On Biomineralization* (Oxford University Press, 1989).
3. S. Amini, A. Miserez, Wear and abrasion resistance selection maps of biological materials. *Acta Biomater.* **9**, 7895–7907 (2013).
4. P. Polygerinos *et al*., Soft robotics: Review of fluid-driven intrinsically soft devices; manufacturing, sensing, control, and applications in human-robot interaction. *Adv. Eng. Mater.* **19**, 1700016 (2017).
5. D. Joester, L. R. Brooker, "The Chiton Radula: A model system for versatile use of iron oxides" in *Iron Oxides: From Nature to Applications*, D. Faivre, Ed. (Wiley-VCH Verlag GmbH & Co. KGaA, 2016), pp. 177–206.
6. L. R. Brooker, J. A. Shaw, The chiton radula: A unique model for biomineralization studies. *Adv. Top. Biominer.* **1**, 65–84 (2012).
7. D. Faivre, T. U. Godec, From bacteria to mollusks: The principles underlying the biomineralization of iron oxide materials. *Angew. Chem. Int. Ed. Engl.* **54**, 4728–4747 (2015).
8. Vichigh Marine, "Gumboot Chiton: Raw video for Matt 1" (video recording, 2015). https://www.youtube.com/watch?v=8JqgCXsq1OM. Accessed 11 May 2021.
9. M. Mizzaro-Wimmer, L. Salvini-Plawen, *Praktische Malakologie: Beiträge zur vergleichend-anatomischen Bearbeitung der Mollusken: Caudofoveata bis Gastropoda—* Streptoneura* (Springer-Verlag, 2013).
10. L. Plate, Die Anatomie und Phylogenie der Chitonen, Teil C. *Zool. Jahrb. Abt. Anat. Ontogenie Tiere* **5**, 281–600 (1901).
11. R. E. Golding, W. F. Ponder, M. Byrne, Three-dimensional reconstruction of the odontophoral cartilages of Caenogastropoda (Mollusca: Gastropoda) using micro-CT: Morphology and phylogenetic significance. *J. Morphol.* **270**, 558–587 (2009).
12. H. Eigenbrodt, Untersuchungen über die Funktion der Radula einiger Schnecken. *Z. Morphol. Ökol. Tiere* **37**, 735–791 (1941).
13. J. A. Shaw, D. J. Macey, L. R. Brooker, P. L. Clode, Tooth use and wear in three iron-biomineralizing mollusc species. *Biol. Bull.* **218**, 132–144 (2010).
14. J. A. Shaw, D. J. Macey, L. R. Brooker, Radula synthesis by three species of iron mineralizing molluscs: Production rate and elemental demand. *J. Mar. Biol. Assoc. U. K.* **88**, 597–601 (2008).
15. N. W. Runham, A study of the replacement mechanism of the pulmonate radula. *J. Cell Sci.* **3**, 271–277 (1963).
16. N. W. Runham, The histochemistry of the radulas of acanthochitona communis, Lymnaea stagnalis, helix pomatia, scaphander lignarius and Archidoris pseudoargus. *Ann. Histochim.* **8**, 433–441 (1963).
17. J. C. Weaver *et al*., Analysis of an ultra hard magnetic biomineral in chiton radular teeth. *Mater. Today* **13**, 42–52 (2010).
18. J. L. Kirschvink, H. A. Lowenstam, Mineralization and magnetization of chiton teeth: Paleomagnetic, sedimentologic, and biologic implications of organic magnetite. *Earth Planet. Sci. Lett.* **44**, 193–204 (1979).
19. L. A. Evans, D.J. Macey, J. Webb, Characterization and structural organization of the organic matrix of the radula teeth of the chiton *Acanthopleura hirtosa*. *Philos. Trans. R. Soc. B* **329**, 87 (1990).
20. P. van der Wal, H. J. Giesen, J. J. Videler, Radular teeth as models for the improvement of industrial cutting devices. *Mater. Sci. Eng. C* **7**, 129–142 (1999).
21. L. K. Grunenfelder *et al*., Stress and damage mitigation from oriented nanostructures within the radular teeth of *Cryptochiton stelleri*. *Adv. Funct. Mater.* **24**, 6093–6104 (2014).
22. A. Pohl *et al*., Radular stylus of *Cryptochiton stelleri*: A multifunctional lightweight and flexible fiber-reinforced composite. *J. Mech. Behav. Biomed. Mater.* **111**, 103991 (2020).
23. T. G. St. Pierre, L. A. Evans, J. Webb, Non-stoichiometric magnetite and maghemite in the mature teeth of the chiton *Acanthopleura hirtosa*. *Hyperfine Interact.* **71**, 1275–1278 (1992).
24. L. Yan *et al*., Exploration of synchrotron Mössbauer microscopy with micrometer resolution: Forward and a new backscattering modality on natural samples. *J. Synchrotron Radiat.* **19**, 814–820 (2012).
25. M. D. Dyar *et al*., Mössbauer parameters of iron in phosphate minerals. *Am. Mineral.* **99**, 914–942 (2014).
26. L. A. Kalev, L. Niesen, Nuclear resonance scattering study on the spin orientation in an epitaxial layer of Fe_3O_4 on MgO(100). *Phys. Rev. B Condens. Matter Mater. Phys.* **67**, 224403 (2003).
27. C. Delacourt, P. Poizot, D. Bonnin, C. Masquelier, Lithium-insertion mechanism in crystalline and amorphous FePO4·nH2O. *J. Electrochem. Soc.* **156**, A595–A605 (2009).
28. P. Gütlich, E. Bill, A. X. Trautwein, *Mößbauer Spectroscopy and Transition Metal Chemistry* (Springer, 2011).
29. E. Murad, U. Schwertmann, The Mössbauer spectrum of ferrihydrite and its relations to those of other iron oxides. *Am. Mineral.* **65**, 1044–1049 (1980).
30. C. Mikutta *et al*., Synthetic coprecipitates of exopolysaccharides and ferrihydrite. Part I: Characterization. *Geochim. Cosmochim. Acta* **72**, 1111–1127 (2008).
31. X. Châtellier *et al*., Immobilization of P by oxidation of Fe(II) ions leading to nanoparticle formation and aggregation. *Appl. Geochem.* **35**, 325–339 (2013).
32. C. Mikutta, C. Schröder, F. Marc Michel, Total X-ray scattering, EXAFS, and Mössbauer spectroscopy analyses of amorphous ferric arsenate and amorphous ferric phosphate. *Geochim. Cosmochim. Acta* **140**, 708–719 (2014).
33. A. J. Davenport, High resolution in situ XANES investigation of the nature of the passive film on iron in a pH 8.4 borate buffer. *J. Electrochem. Soc.* **142**, 725 (1995).
34. G. Pratesi, C. Ciprani, G. Giuli, W. D. Birch, Santabarbaraite. *Eur. J. Mineral.* **15**, 185–192 (2003).
35. C. Janiak, "Komplex-/ Koordinationschemie" in *Moderne Anorganische Chemie*, C. Janiak, D. Gudat, P. Kurz, H.-J. Meyer, Eds. (Walter de Gruyter GmbH, Berlin, 2018), pp. 381–578.
36. J. H. E. Cartwright, A. G. Checa, J. D. Gale, D. Gebauer, C. I. Sainz-Díaz, Calcium carbonate polyamorphism and its role in biomineralization: How many amorphous calcium carbonates are there?*Angew. Chem. Int. Ed. Engl.* **51**, 11960–11970 (2012).
37. H. A. Lowenstam, Phosphatic hard tissues of marine invertebrates: Their nature and mechanical function, and some fossil implications. *Chem. Geol.* **9**, 153–166 (1972).
38. J. B. Buchanan, B. E. Brown, T. L. Coombs, B. J. S. Pirie, J. A. Allen, The accumulation of ferric iron in the guts of some spatangoid echinoderms. *J. Mar. Biol. Assoc. U. K.* **60**, 631–640 (1980).
39. G. V. Iyengar, L. Tandon, Minor and trace elements in human bones and teeth. https://www.osti.gov/etdeweb/servlets/purl/20067517. Accessed 11 May 2021.
40. A.-C. Senn *et al*., Composition and structure of Fe(III)-precipitates formed by Fe(II) oxidation in water at near-neutral pH. *Geochim. Cosmochim. Acta* **162**, 220–246 (2015).
41. L. M. Gordon *et al*., Dental materials. Amorphous intergranular phases control the properties of rodent tooth enamel. *Science* **347**, 746–750 (2015).
42. L. R. Brooker, A. P. Lee, D. J. Macey, J. Webb, W. van Bronswijk, In situ studies of biomineral deposition in the radula teeth of chitons of the suborder Chitonina. *Venus (Tokyo)* **65**, 71–80 (2006).
43. E. G. Pringsheim, F. E. Fritsch, On iron flagellates. *Philos. Trans. R. Soc. Lond. B Biol. Sci.* **232**, 311–342 (1946).
44. R. H. Hedley, Cement and iron in the arenaceous foraminifera. *Micropaleontology* **9**, 433–441 (1963).
45. D. C. Gillan, C. de Ridder, Morphology of a ferric iron-encrusted biofilm forming on the shell of a burrowing bivalve (Mollusca). *Aquat. Microb. Ecol.* **12**, 1–10 (1997).
46. J. Miot *et al*., Transformation of vivianite by anaerobic nitrate-reducing iron-oxidizing bacteria. *Geobiology* **7**, 373–384 (2009).
47. G. D. Watt, R. B. Frankel, G. C. Papaefthymiou, K. Spartalian, E. I. Stiefel, Redox properties and Moessbauer spectroscopy of Azotobacter vinelandii bacterioferritin. *Biochemistry* **25**, 4330–4336 (1986).
48. V. J. Wade *et al*., Structure and composition of ferritin cores from pea seed (Pisum sativum). *Biochim. Biophys. Acta* **1161**, 91–96 (1993).
49. J. Baumgartner *et al*., Magnetotactic bacteria form magnetite from a phosphate-rich ferric hydroxide via nanometric ferric (oxyhydr)oxide intermediates. *Proc. Natl. Acad. Sci. U.S.A.* **110**, 14883–14888 (2013).
50. J. F. V. Vincent, U. G. K. Wegst, Design and mechanical properties of insect cuticle. *Arthropod Struct. Dev.* **33**, 187–199 (2004).
51. D. Raabe, C. Sachs, P. Romano, The crustacean exoskeleton as an example of a structurally and mechanically graded biological nanocomposite material. *Acta Mater.* **53**, 4281–4292 (2005).
52. B. H. M. Seidl *et al*., Tailored disorder in calcite organization in tergite cuticle of the supralittoral isopod Tylos europaeus Arcangeli, 1938. *J. Struct. Biol.* **204**, 464–480 (2018).
53. E. S. Greenhalgh, *Failure Analysis and Fractography of Polymer Composites* (Woodhead, 2009).
54. E. D. Sone, S. Weiner, L. Addadi, Biomineralization of limpet teeth: A cryo-TEM study of the organic matrix and the onset of mineral deposition. *J. Struct. Biol.* **158**, 428–444 (2007).
55. H.-O. Fabritius, C. Sachs, P. R. Triguero, D. Raabe, Influence of structural principles on the mechanics of a biological fiber-based composite material with hierarchical organization: The exoskeleton of the lobster *Homarus americanus*. *Adv. Mater.* **21**, 391–400 (2009).
56. Y. Politi, B. Bar-On, H.-O. Fabritius, "Mechanics of arthropod cuticle-versatility by structural and compositional variation" in *Architectured Materials in Nature and Engineering: Archimats*, Y. Estrin, Y. Bréchet, J. Dunlop, P. Fratzl, Eds. (Springer International Publishing, 2019), pp. 287–327.
57. B. Seidl *et al*., Ultrastructure and mineral distribution in the tergite cuticle of the beach isopod Tylos europaeus Arcangeli, 1938. *J. Struct. Biol.* **174**, 512–526 (2011).

Downloaded at Universiteit Gent on June 10, 2021

58. F. W. Zok, A. Miserez, Property maps for abrasion resistance of materials. *Acta Mater.* **55**, 6365–6371 (2007).
59. S. El-Safty, R. Akhtar, N. Silikas, D. C. Watts, Nanomechanical properties of dental resin-composites. *Dent. Mater.* **28**, 1292–1300 (2012).
60. L. D. Randolph, W. M. Palin, G. Leloup, J. G. Leprince, Filler characteristics of modern dental resin composites and their influence on physico-mechanical properties. *Dent. Mater.* **32**, 1586–1599 (2016).
61. J. A. Shaw, *Biomineralisation Processes in the Radula Teeth of the Chiton Acanthopleura Hirtosa* (Murdoch University, Western Australia, Australia, 2007).
62. W. C. Oliver, G. M. Pharr, Measurement of hardness and elastic modulus by instrumented indentation. *J. Mater. Res.* **19**, 3–20 (2004).
63. C. A. Schneider, W.S. Rasband, K.W. Eliceiri, NIH image to imageJ: 25 years of image analysis. *Nat. Methods* **9**, 671–675 (2012).
64. P. Sikorski, R. Hori, M. Wada, Revisit of α-chitin crystal structure using high resolution X-ray diffraction data. *Biomacromolecules* **10**, 1100–1105 (2009).
65. S. R. Sutton *et al.*, Spatially resolved elemental analysis, spectroscopy and diffraction at the GSECARS sector at the advanced photon source. *J. Environ. Qual.* **46**, 1158–1165 (2017).
66. S. Kraft, J. Stümpel, P. Becker, U. Kuetgens, High resolution x-ray absorption spectroscopy with absolute energy calibration for the determination of absorption edge energies. *Rev. Sci. Instrum.* **67**, 681–687 (1996).
67. B. Ravel, M. Newville, Athena, artemis, hephaestus: Data analysis for X-ray absorption spectroscopy using IFEFFIT. *J. Synchrotron Radiat.* **12**, 537–541 (2005).
68. M. Newville, Larch: An analysis package for XAFS and related spectroscopies. *J. Phys. Conf. Ser.* **430**, 12007 (2013).
69. M. Newville, T. Stensitzki, D. B. Allen, A. Ingargiola, Data from "LMFIT: Non-linear least-square minimization and curve-fitting for Python."*Zenodo*. https://doi.org/10.5281/zenodo.11813. Accessed 11 May 2021.
70. M. Wilke, F. Farges, P.-E. Petit, G. E. Brown, F. Martin, Oxidation state and coordination of Fe in minerals. *Am. Mineral.* **86**, 714–730 (2001).
71. W. Sturhahn, CONUSS and PHOENIX. *Hyperfine Interact.* **125**, 149–172 (2000).
72. F. Croisier, C. Jérôme, Chitosan-based biomaterials for tissue engineering. *Eur. Polym. J.* **49**, 780–792 (2013).
73. A. Toffey, G. Samaranayake, C. E. Frazier, W. G. Glasser, Chitin derivatives. I. Kinetics of the heat-induced conversion of chitosan to chitin. *J. Appl. Polym. Sci.* **60**, 75–85 (1996).

Downloaded at Universiteit Gent on June 10, 2021